Title

Structural basis of SARS-CoV-2 Omicron immune evasion and receptor engagement

Journal

Science, 375(6583)

ISSN

0036-8075

Authors

McCallum, Matthew

Czudnochowski, Nadine

Rosen, Laura E

et al.

Publication Date

2022-02-25

DOI

10.1126/science.abn8652

Peer reviewed

CORONAVIRUS

Structural basis of SARS-CoV-2 Omicron immune evasion and receptor engagement

Matthew McCallum[1]†, Nadine Czudnochowski[2]†, Laura E. Rosen[2], Samantha K. Zepeda[1], John E. Bowen[1], Alexandra C. Walls[1,3], Kevin Hauser[2], Anshu Joshi[1], Cameron Stewart[1], Josh R. Dillen[2], Abigail E. Powell[2], Tristan I. Croll[4], Jay Nix[5], Herbert W. Virgin[2,6,7], Davide Corti[8], Gyorgy Snell[2]*, David Veesler[1,3]*

The severe acute respiratory syndrome coronavirus 2 (SARS-CoV-2) Omicron variant of concern evades antibody-mediated immunity that comes from vaccination or infection with earlier variants due to accumulation of numerous spike mutations. To understand the Omicron antigenic shift, we determined cryo–electron microscopy and x-ray crystal structures of the spike protein and the receptor-binding domain bound to the broadly neutralizing sarbecovirus monoclonal antibody (mAb) S309 (the parent mAb of sotrovimab) and to the human ACE2 receptor. We provide a blueprint for understanding the marked reduction of binding of other therapeutic mAbs that leads to dampened neutralizing activity. Remodeling of interactions between the Omicron receptor-binding domain and human ACE2 likely explains the enhanced affinity for the host receptor relative to the ancestral virus.

Although sequential COVID-19 waves have swept the world, no variants have accumulated mutations and mediated immune evasion to the extent observed for the severe acute respiratory syndrome coronavirus 2 (SARS-CoV-2) Omicron (B.1.1.529) variant of concern (VOC). This variant was first identified in late November 2021 in South Africa and was quickly designated a VOC by the World Health Organization (*1*). Omicron has spread worldwide at a rapid pace relative to previous SARS-CoV-2 variants (*2*, *3*). The Omicron spike (S) glycoprotein, which promotes viral entry into cells (*4*, *5*), harbors 37 residue mutations in the predominant haplotype relative to Wuhan-Hu-1 S (*4*), whereas SARS-CoV-2 Alpha and Delta VOC display ~10 substitutions (*2*, *6*). The Omicron receptor-binding domain (RBD) and N-terminal domain (NTD) contain 15 and 11 mutations, respectively, which lead to severe dampening of plasma-neutralizing activity in previously infected or vaccinated individuals (*7*–*11*). Although the Omicron RBD harbors 15 residue mutations, it binds to the human ACE2 entry receptor with high affinity and can efficiently recognize mouse ACE2 (*7*). As a result of this antigenic shift, the only authorized or approved therapeutic monoclonal antibodies (mAbs) with neutralizing activity against Omicron are S309 (sotrovimab parent) and the COV2-2196/COV2-2130 cocktail (cilgavimab/tixagevimab parents). Even these mAbs had reduced potency (by a factor of 2 to 3 and by a factor of 12 to 200, respectively), according to pseudovirus or authentic virus assays (*7*–*11*). This extent of evasion of humoral responses has important consequences for therapy and prevention of both the current pandemic and future pandemics.

To define the molecular mechanisms involved in Omicron immune evasion and altered receptor recognition, we determined cryo–electron microscopy (cryo-EM) structures of the prefusion-stabilized SARS-CoV-2 Omicron S ectodomain trimer bound to S309 and S2L20 (NTD-specific mAb) Fab fragments (Fig. 1, fig. S1, and table S1) and the x-ray crystal structure of the Omicron RBD in complex with human ACE2 and the Fab fragments of S309 and S304 at 2.85 Å resolution (table S2). S309 recognizes antigenic site IV (*12*), whereas S304 binds to site

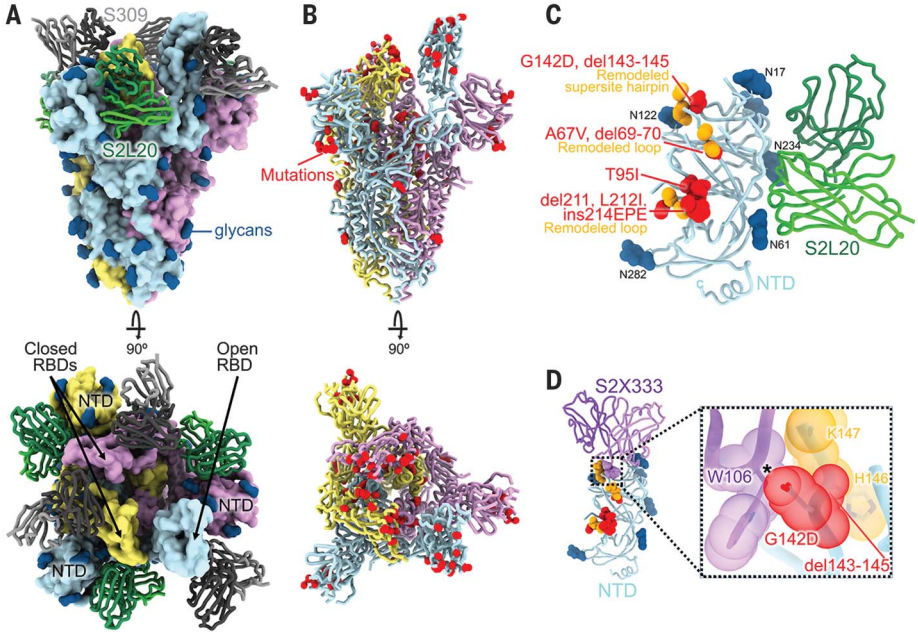

Fig. 1. Cryo-EM structure of the SARS-CoV-2 Omicron S trimer reveals a remodeling of the NTD antigenic supersite. (**A**) Surface rendering in two orthogonal orientations of the Omicron S trimer with one open RBD bound to the S309 (gray) and S2L20 (green) Fabs shown as ribbons. The three S protomers are colored light blue, pink, and gold. N-linked glycans are shown as dark blue surfaces. (**B**) Ribbon diagrams in two orthogonal orientations of the S trimer with one open RBD. Omicron residues mutated relative to Wuhan-Hu-1 are shown as red spheres (except D614G, which is not shown). (**C**) The S2L20-bound Omicron NTD with mutated, deleted, or inserted residues rendered or indicated as red spheres. Segments with notable structural changes are shown in orange and labeled. (**D**) Zoomed-in view of the Omicron NTD antigenic supersite overlaid with the S2X333 Fab [used here as an example of a prototypical NTD-neutralizing mAb (*22*)], highlighting the binding incompatibility; the modeled clash between S2X333 Trp^{106} and NTD G142D is indicated with an asterisk.

[1]Department of Biochemistry, University of Washington, Seattle, WA 98195, USA. [2]Vir Biotechnology, San Francisco, CA 94158, USA. [3]Howard Hughes Medical Institute, University of Washington, Seattle, WA 98195, USA. [4]Cambridge Institute for Medical Research, Department of Haematology, University of Cambridge, Cambridge, UK. [5]Molecular Biology Consortium, Advanced Light Source, Lawrence Berkeley National Laboratory, Berkeley, CA, USA. [6]Department of Pathology and Immunology, Washington University School of Medicine, St. Louis, MO 63110, USA. [7]Department of Internal Medicine, UT Southwestern Medical Center, Dallas, TX 75390, USA. [8]Humabs Biomed SA, a subsidiary of Vir Biotechnology, 6500 Bellinzona, Switzerland.
***Corresponding author. Email: dveesler@uw.edu (D.V.); gsnell@vir.bio (G.S.)**
†These authors contributed equally to this work.

IIc (*13*) and was used to assist crystallization. Furthermore, we used surface plasmon resonance (SPR) to evaluate the binding of clinical mAbs to the Omicron RBD and S ectodomain trimer.

Three-dimensional classification of the cryo-EM data revealed the presence of two conformational states with one (45% of selected particles) or two (55% of selected particles) RBDs in the open conformation, for which we determined structures at 3.1 Å and 3.2 Å resolution, respectively (Fig. 1, A and B, figs. S1 and S2, and table S1). The larger fraction of open RBDs, relative to the apo (*4*, *5*) and S309-bound (*12*) Wuhan-Hu-1 S ectodomain trimer structures, could result from the Omicron mutations, the prefusion-stabilizing mutations (*14*, *15*), or S2L20 binding. Focused classification and local refinement of the S309-bound RBD (domain B) and of the S2L20-bound NTD (domain A) were used to account for their conformational dynamics and led to improved local resolution of these regions (to 3.0 and 3.3 Å resolution, respectively).

Whereas most VOCs have only a few mutations beyond the NTD, RBD, and furin cleavage site regions, the Omicron spike harbors eight substitutions outside of these areas: T547K, H655Y, N764K, D796Y, N856K, Q954H, N969K, and L981F, which could all be modeled in the map (Fig. 1, A and B, and Fig. 2). Three of these mutations introduce interprotomer electrostatic contacts between the S_2 and S_1 subunits: N764K binds Gln^{314} (in domain D), Ser^{982} binds T547K (in domain C of protomers with closed RBDs), and N856K binds Asp^{568} and Thr^{572} (in domain C, the former residue is closer to N856K in protomers with closed RBDs) (Fig. 2) (*16*, *17*). Furthermore, N969K forms interprotomer electrostatic contacts with Q755, and L981F improves intraprotomer hydrophobic packing in the prefusion conformation (Fig. 2). The latter mutation is close to the prefusion-stabilizing 2P mutations (K986P and V987P) used in all three vaccines deployed in the US (Fig. 2). Consistent with recent studies (*18*–*20*), S_1 shedding might be reduced by enhanced interactions between the S_1 and S_2 subunits in Omicron S along with prefusion stabilization, or by altered processing at the S_1-S_2 cleavage site due to the N679K and P681H mutations. Dampened S_1 subunit shedding might enhance the effector function activity of vaccine- or infection-elicited Abs along with that of therapeutic mAbs (*21*) that retain affinity for Omicron S.

The Omicron NTD carries numerous mutations, deletions (del), and an insertion (ins) including A67V, del69-70, T95I, G142D, del143-145, del211, L212I, and ins214EPE (Fig. 1C and fig. S3). Many of these mutations have been described in previously emerged VOCs: del69-70 was found in Alpha, T95I was present in Kappa and Iota, and G142D was present in Kappa and Delta. T95I, del211, L212I, and ins214EPE are outside the NTD antigenic supersite but in the vicinity of the epitope targeted by the P008_056 mAb, which suggests that these mutations could putatively modulate recognition of similar mAbs or have another functional relevance. Although the region comprising del143-145 is weakly resolved in the map, it is expected to alter antibody recognition as a result of the introduced sequence register shift, whereas G142D is incompatible with binding of several potent NTD-neutralizing mAbs (such as S2X333) because of steric hindrance (Fig. 1D) (*2*, *22*). Moreover, del143-145 is reminiscent of Alpha del144, which was also isolated as an escape mutation in the presence of mAb S2X333 and led to viral breakthrough in a hamster challenge model (*22*). These data suggest that G142D and del143-145 account for the observed SARS-CoV-2 Omicron evasion

Table 1. Omicron RBD mutations with a demonstrated (X) or expected (x) reduction of binding or neutralization and based on our structural analyses.
Total GISAID counts are as of 9 January 2022. Entries with >5% Ns are excluded; n/a, not applicable. VOI, variant of interest; VUM, variant under monitoring.

	REGN10933	REGN10987	COV2-2196	COV2-2130	LY-CoV555	LY-CoV016	CT-P59	S309	ADI-58125	Total GISAID counts	Omicron counts	VOC, VOI, VUM harboring mutation
G339D										196,756	192,125	
S371L										182,692	179,486	
S373P										185,025	181,374	
S375F										184,990	181,461	
K417N	X					X	X			116,510	70,903	Beta, K417T in Gamma
N440K										92,338	79,859	
G446S		X		x						83,953	80,518	
S477N	x		X			x				262,216	187,081	
T478K			X							3,976,461	187,859	Delta
E484A	X			X	X		X			192,062	186,965	E484K in Beta, Gamma, Mu, Iota, Eta, Zeta, Theta; E484Q in Kappa
Q493R	X		X	x	X	x	X			191,484	188,353	
G496S							X			187,583	184,575	
Q498R							X			188,462	185,805	
N501Y										1,434,752	186,285	Alpha, Beta, Theta, N501K in Mu
Y505H									X*	188,250	185,491	
PDB ID	6XDG	6XDG	7L7D	7L7E	7KMG	7C01	7CM4	This study	n/a			

*For ADI-58125, the impact on binding of C, N, and S substitutions is shown at position Tyr^{505} according to mutagenesis studies [J. Belk *et al*., WO2021207597 - Compounds Specific to Coronavirus S Protein and Uses Thereof. Adagio Therapeutics Inc. (2021)].

from neutralization mediated by a panel of NTD mAbs (*7*, *9*).

The RBD is the main target of plasma-neutralizing activity in convalescent and vaccinated individuals and comprises several antigenic sites recognized by neutralizing Abs with a range of neutralization potencies and breadth (*12*, *13*, *21*, *23*–*36*) (Fig. 3A). Our structures provide a high-resolution blueprint of the residue substitutions found in this variant (Fig. 3B) and their impact on binding of clinical mAbs (Table 1). Several individual mutations or subsets of mutations occurring in the Omicron RBD have been reported to affect neutralizing antibody binding or neutralization (*37*). The K417N, G446S, S477N, T478K, E484A, Q493R, G496S, Q498R, N501Y. and Y505H mutations are part of antigenic site I, which is immunodominant in previous variants (*13*, *24*). K417N, E484A, S477N, and Q493R would lead to loss of electrostatic interactions and steric clashes with REGN10933 whereas G446S would lead to steric clashes with REGN10987, consistent with the dampened binding to the Omicron RBD and S trimer (Fig. 3, C and D, fig. S3, and table S3) and with previous analyses of the impact of individual mutations on neutralization by each of these two mAbs (*9*, *38*–*40*). Moreover, N440K was reported to dampen REGN10987 neutralization severely (*9*). Reduced binding of the Omicron RBD to COV2-2196 and COV2-2130, relative to the Wuhan-Hu-1 RBD, likely results from T478K [based on Delta S (*2*)], Q493R, and putatively S477N for COV2-2196, as well as G446S and E484A for COV2-2130 (Fig. 3, E and F, fig. S4, and table S3). Integrating these data with neutralization assays suggests that although each point mutation only imparts a small reduction of COV2-2196– or COV2-2130–mediated neutralization (*9*), the constellation of Omicron mutations leads to more pronounced loss of activity (*7*–*11*). E484A abrogates electrostatic interactions with LY-CoV555 heavy and light chains, whereas Q493R would prevent binding through steric hindrance (Fig. 3G, fig. S4, and table S3), as supported by neutralization data (*9*). K417N is expected to negatively affect the constellation of electrostatic interactions formed between the Omicron RBD and LY-CoV16 heavy chain, thereby abolishing binding (Fig. 3H, fig. S4, and table S3) and neutralization of single-mutant S pseudoviruses (*9*, *40*, *41*). Furthermore, S477N and Q493R have been shown to dampen binding of and neutralization mediated by LY-CoV16 (*9*, *41*). Finally, K417N, E484A, and Q493R hinder CT-P59 engagement through a combination of steric hindrance and remodeling of electrostatic contacts, thereby preventing binding (Fig. 3I, fig. S4, and tables S1 and S3).

The SARS-CoV-2 Omicron G339D and N440K mutations are within or near antigenic site IV, which is recognized by the S309 mAb (*12*). Nonetheless, relative to Wuhan-Hu-1 pseudovirus or Washington-1 authentic virus, S309 undergoes only a factor of 2 to 3 reduction of neutralizing activity against Omicron (*7*, *9*–*11*). The Lys side chain introduced by the N440K substitution points away from the S309 epitope and does not affect binding. The Asp side chain introduced by the G339D substitution does not interfere with the S309 epitope, although not all rotamers are compatible with mAb binding (fig. S2). This finding likely explains the similarly moderate reduction of S309 potency against the single G339D S mutant (*9*) or the full constellation of Omicron S mutations (*7*, *9*–*11*). The modest reduction of the Omicron RBD binding to S309 (Fig. 3J, fig. S4, and table S3) mirrors the reduced neutralization potency of this VOC (by a factor of 2 to 3 relative to ancestral viruses) and concurs with deep-mutational scanning analysis of individual mutations on S309 recognition (*24*). Overall, the S309 binding mode remains unaltered by the Omicron mutations, including recognition of the N343 glycan (fig. S5).

The Omicron RBD is structurally similar to the Wuhan-Hu-1 RBD, and both structures can be superimposed with an RMSD of 0.8 Å over 183 aligned Cα residues [as compared to PDB 6m0j (*42*)]. However, the region comprising residues *366* to *375*, which harbors the S371L/S373P/S375F substitutions, deviates markedly from the conformation observed for the Wuhan-Hu-1 RBD, irrespective of the presence of bound linoleic acid (*4*, *42*, *43*). Although this region is weakly resolved in the cryo-EM and x-ray structures, the conformation adopted in the latter structure is incompatible with binding of some cross-reactive site II mAbs such as S2X35, consistent with our observation of dampened binding (fig. S6). We therefore propose that these mutations participate in rendering this region of the RBD dynamic and mediate immune evasion from some site II mAbs.

We recently reported that the SARS-CoV-2 Omicron RBD binds human ACE2 with a factor of ~2.4 enhanced affinity relative to the Wuhan-Hu-1 RBD (*7*). Our crystal structure of the human ACE2-bound Omicron RBD elucidates how the constellation of RBD mutations found in this VOC affect receptor recognition

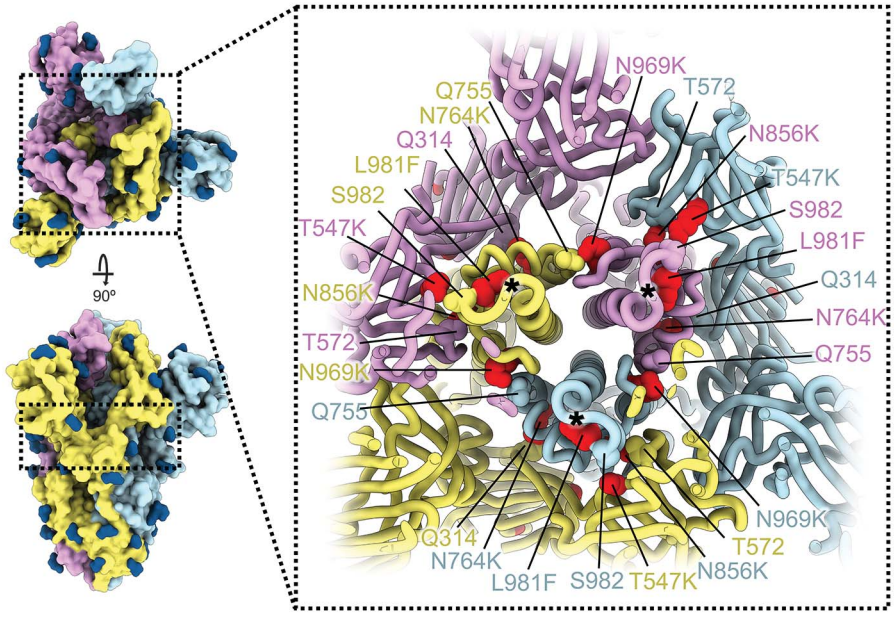

Fig. 2. SARS-CoV-2 Omicron S mutations outside the NTD and RBD. Ribbon diagram shows a cross section of the Omicron S glycoprotein (the location of this slice on the S trimer is indicated at left). Mutated residues T547K, N764K, N856K, N969K, and L981F are shown as red spheres, whereas the residues they contact are shown as spheres colored as the protomer to which they belong. Black asterisks show the positions of residues involved in the prefusion-stabilizing 2P mutations (K986P and V987P) used in all three vaccines deployed in the US. The three S protomers are colored light blue, pink, and gold. N-linked glycans are shown as dark blue surfaces.

(Fig. 4A and table S2). The N501Y mutation alone enhances ACE2 binding to the RBD by a factor of 6 relative to the Wuhan-Hu-1 RBD, as reported for the Alpha variant (*6*), likely as a result of increased shape complementarity between the introduced Tyr side chain and the ACE2 Tyr^{41} and Lys^{353} side chains (Fig. 4B). Omicron S residue Tyr^{501} and ACE2 residue Tyr^{41} form a T-shaped π-π stacking interaction, as previously observed for an N501Y-harboring S structure in complex with ACE2 (*44*). The K417N mutation dampens receptor recognition by a factor of ~3 (*2*, *6*, *39*, *45*) likely through loss of a salt bridge with ACE2 Asp^{30} (Fig. 4C). The Q493R and Q498R mutations introduce two new salt bridges with Glu^{35} and Glu^{38}, respectively, replacing hydrogen bonds formed with the Wuhan-Hu-1 RBD and thereby remodeling the electrostatic interactions with ACE2 (Fig. 4D). Both of these individual mutations were reported to reduce ACE2 binding avidity slightly by deep-mutational scanning studies of the yeast-displayed SARS-CoV-2 RBD (*46*). Finally, S477N leads to formation of new hydrogen bonds between the introduced Asn side chain and the ACE2 Ser^{19} backbone amine and carbonyl groups (Fig. 4E). Collectively, these mutations have a net enhancing effect on binding of the Omicron RBD to human ACE2 relative to Wuhan-Hu-1, which suggests that structural epistasis enables immune evasion while retaining efficient receptor engagement. The large number of Omicron mutations in the immunodominant receptor-binding motif likely explains a substantial proportion of the loss of neutralization by convalescent and vaccine-elicited polyclonal antibodies, and is in line with the known plasticity of this subdomain (*24*).

Although the N501Y mutation has previously been described as enabling some SARS-CoV-2 VOCs to infect and replicate in mice, the Alpha and Beta variant RBDs only weakly bound mouse ACE2 (*47*, *48*). The SARS-CoV-2 Omicron RBD, however, interacts more strongly with mouse ACE2 than do the Alpha and Beta variant RBDs when evaluated side-by-side (fig. S7A) and can use mouse ACE2 as an entry receptor for S-mediated entry (*7*, *49*). We propose that the Q493R mutation plays a key role in enabling efficient mouse ACE2 binding, which occurs through formation of a new electrostatic interaction with the Asn^{31} side chain amide (Lys^{31} in human ACE2); this is supported by in silico modeling based on our human ACE2-bound crystal structure (fig. S7B). These findings concur with the emergence and fixation of the Q493K RBD mutation upon serial passaging in mice to yield a mouse-adapted virus designated SARS-CoV-2 MA10 (*50*).

This work defines the molecular basis for the broad evasion of humoral immunity exhibited

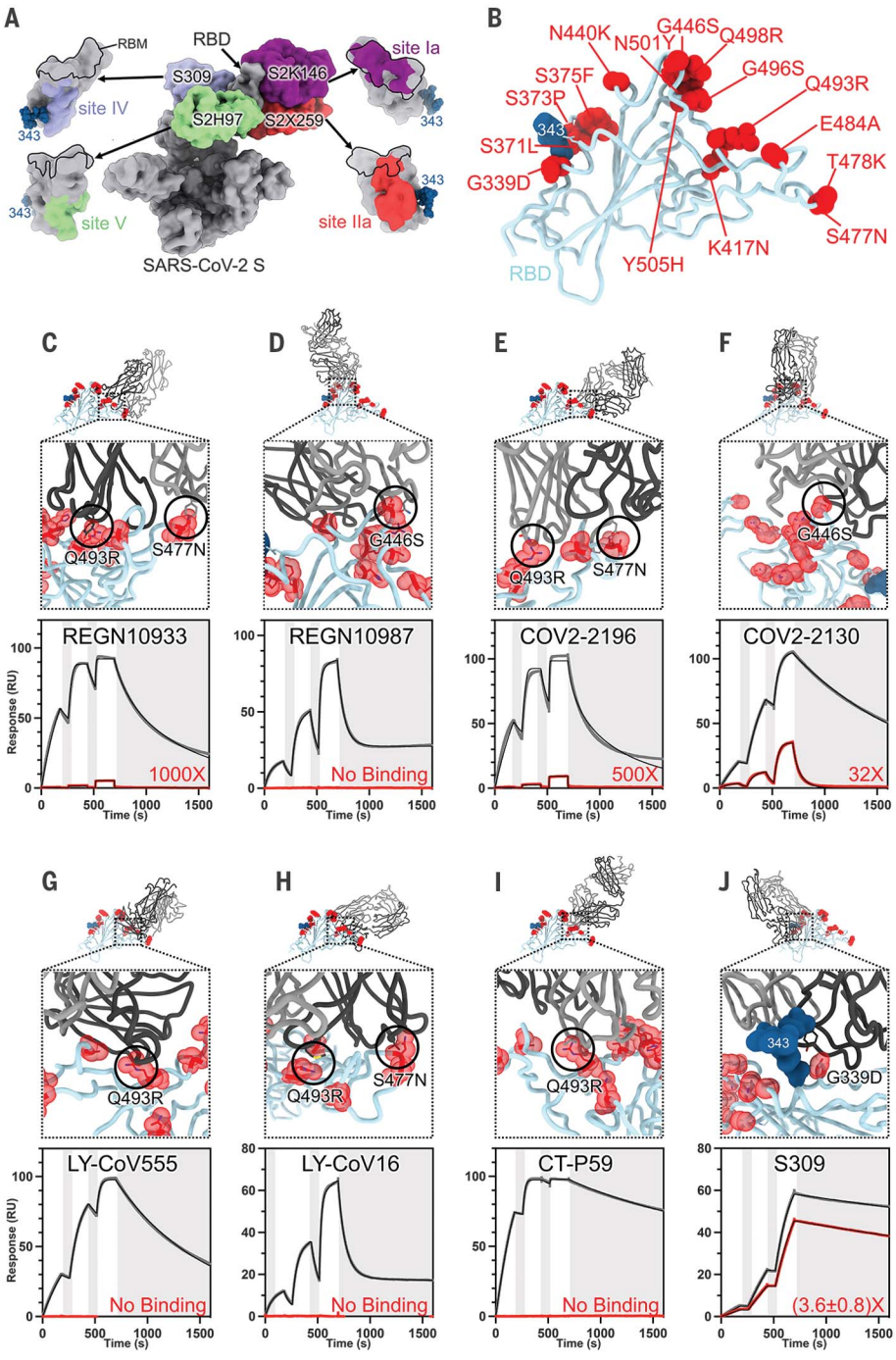

Fig. 3. SARS-CoV-2 Omicron RBD mutations promote escape from a panel of clinical mAbs. (**A**) RBD antigenic map as determined in (*13*). (**B**) Ribbon diagram of the RBD crystal structure, with residues mutated relative to the Wuhan-Hu-1 RBD shown as red spheres. The N343 glycan is rendered as blue spheres. (**C** to **J**) Zoomed-in views of the Omicron RBD (blue) superimposed on structures of clinical mAbs (gray). Selected residues that interfere with the following mAbs are circled: (C) REGN10933, (D) REGN10987, (E) COV2-2196, (F) COV2-2130, (G) LY-CoV555, (H) LY-CoV16, (I) CT-P59, and (J) S309, which does not clash with G339D. All panels were rendered with the crystal structure except (J), which was generated with the cryo-EM model. Binding of the Wuhan-Hu-1 (gray line) or Omicron (red line) RBD to the corresponding mAb was evaluated using surface plasmon resonance (single-cycle kinetics) and is shown underneath each structural superimposition. White and gray stripes are association and dissociation phases, respectively. The thin black line is a fit to a kinetic model. The decrease in affinity between Wuhan-Hu-1 and Omicron binding is indicated in red. Results are consistent with immunoglobulin G binding to S ectodomains (fig. S3).

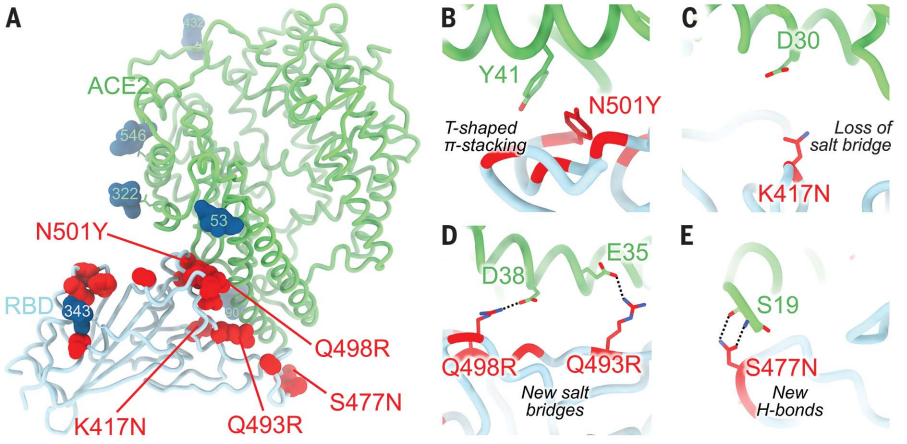

Fig. 4. Molecular basis of human ACE2 recognition by the SARS-CoV-2 Omicron RBD. (**A**) Ribbon diagram of the crystal structure of the Omicron RBD in complex with the ACE2 ectodomain. The S309 and S304 Fab fragments are not shown for clarity. (**B** to **E**) Zoomed-in views of the RBD-ACE2 interface. highlighting modulation of interactions due to introduction of the N501Y (B), K417N (C), Q493R/Q498R (D), and S477N (E) residue substitutions.

by SARS-CoV-2 Omicron and underscores the SARS-CoV-2 S mutational plasticity as well as the importance of targeting conserved epitopes in the design and development of vaccines and therapeutics. The S309 mAb (the parent of sotrovimab) neutralizes Omicron with one-half to one-third the potency with which it neutralizes Wuhan-Hu-1 or Washington-1, whereas the seven other clinical mAbs or mAb cocktails undergo reduction of neutralizing activity of one to two orders of magnitude or greater. Furthermore, some Omicron isolates (≈9%) harbor the R346K substitution, which, in conjunction with N440K (present in the main haplotype), leads to escape from C135 mAb-mediated neutralization (*25*, *51*). R346K does not affect S309 whether in isolation or in the context of the full constellation of Omicron mutations; hence, mAbs targeting antigenic site IV can be differently affected by Omicron (*7*, *9*, *46*). Whereas C135 was identified from a SARS-CoV-2 convalescent donor (*25*), S309 was isolated from a subject who recovered from a SARS-CoV infection in 2003 (*12*); the latter strategy increased the likelihood of finding mAbs that recognize epitopes that are mutationally constrained throughout sarbecovirus evolution. The identification of broadly reactive mAbs that neutralize multiple distinct sarbecoviruses, including SARS-CoV-2 variants, paves the way for designing vaccines that elicit broad sarbecovirus immunity (*52*–*56*). These efforts offer hope that the same strategies that contribute to solving the current pandemic will prepare us for possible future sarbecovirus pandemics.

REFERENCES AND NOTES

1. R. Viana *et al.*, *Nature* 10.1038/s41586-022-04411-y (2022).
2. M. McCallum *et al.*, *Science* **374**, 1621–1626 (2021).
3. M. McCallum *et al.*, *Science* **373**, 648–654 (2021).
4. A. C. Walls *et al.*, *Cell* **181**, 281–292.e6 (2020).
5. D. Wrapp *et al.*, *Science* **367**, 1260–1263 (2020).
6. D. A. Collier *et al.*, *Nature* **593**, 136–141 (2021).
7. E. Cameroni *et al.*, *Nature* 10.1038/s41586-021-04386-2 (2021).
8. Y. Cao *et al.*, *Nature* 10.1038/s41586-021-04385-3 (2021).
9. L. Liu *et al.*, *Nature* 10.1038/s41586-021-04388-0 (2021).
10. D. Planas *et al.*, *Nature* 10.1038/s41586-021-04389-z (2021).
11. L. A. VanBlargan *et al.*, bioRxiv 472828 [preprint] (2021).
12. D. Pinto *et al.*, *Nature* **583**, 290–295 (2020).
13. L. Piccoli *et al.*, *Cell* **183**, 1024–1042.e21 (2020).
14. C. L. Hsieh *et al.*, *Science* **369**, 1501–1505 (2020).
15. E. Olmedillas *et al.*, bioRxiv 441046 [preprint] (2021).
16. A. C. Walls *et al.*, *Nature* **531**, 114–117 (2016).
17. M. A. Tortorici, D. Veesler, *Adv. Virus Res.* **105**, 93–116 (2019).
18. Z. Cong *et al.*, bioRxiv 472934 [preprint] (2021).
19. B. Meng *et al.*, bioRxiv 473248 [preprint] (2021).
20. K. Sato *et al.*, Research Square 10.21203/rs.3.rs-1207670/v1 [preprint] (2022).
21. M. A. Tortorici *et al.*, *Nature* **597**, 103–108 (2021).
22. M. McCallum *et al.*, *Cell* **184**, 2332–2347.e16 (2021).
23. L. Stamatatos *et al.*, *Science* **372**, 1413–1418 (2021).
24. T. N. Starr *et al.*, *Nature* **597**, 97–102 (2021).
25. C. O. Barnes *et al.*, *Nature* **588**, 682–687 (2020).
26. C. A. Jette *et al.*, *Cell Rep.* **36**, 109760 (2021).
27. C. O. Barnes *et al.*, *Cell* **182**, 828–842.e16 (2020).
28. S. J. Zost *et al.*, *Nature* **584**, 443–449 (2020).
29. D. R. Martinez *et al.*, *Sci. Transl. Med.* eabj7125 (2021).
30. J. Dong *et al.*, *Nat. Microbiol.* **6**, 1233–1244 (2021).
31. A. J. Greaney *et al.*, *Sci. Transl. Med.* **13**, eabi9915 (2021).
32. J. Hansen *et al.*, *Science* **369**, 1010–1014 (2020).
33. C. G. Rappazzo *et al.*, *Science* **371**, 823–829 (2021).
34. A. Z. Wec *et al.*, *Science* **369**, 731–736 (2020).
35. Y.-J. Park *et al.*, *Science* eabm8143 (2022).
36. J. E. Bowen *et al.*, bioRxiv 473391 [preprint] (2021).
37. D. Corti, L. A. Purcell, G. Snell, D. Veesler, *Cell* **184**, 3086–3108 (2021).
38. T. Tada *et al.*, *mBio* **12**, e0069621 (2021).
39. M. Yuan *et al.*, *Science* **373**, 818–823 (2021).
40. P. Wang *et al.*, *Nature* **593**, 130–135 (2021).
41. T. N. Starr *et al.*, *Science* **371**, 850–854 (2021).
42. J. Lan *et al.*, *Nature* **581**, 215–220 (2020).
43. C. Toelzer *et al.*, *Science* **370**, 725–730 (2020).
44. X. Zhu *et al.*, *PLOS Biol.* **19**, e3001237 (2021).
45. E. C. Thomson *et al.*, *Cell* **184**, 1171–1187.e20 (2021).
46. T. N. Starr *et al.*, *Cell* **182**, 1295–1310.e20 (2020).
47. H. Shuai *et al.*, *EBioMedicine* **73**, 103643 (2021).
48. T. Pan *et al.*, *Signal Transduct. Target. Ther.* **6**, 420 (2021).
49. M. Hoffmann *et al.*, *Cell* 10.1016/j.cell.2021.12.032 (2022).
50. S. R. Leist *et al.*, *Cell* **183**, 1070–1085.e12 (2020).
51. Y. Weisblum *et al.*, *eLife* **9**, e61312 (2020).
52. A. C. Walls *et al.*, *Cell* **184**, 5432–5447.e16 (2021).
53. A. C. Walls *et al.*, *Cell* **183**, 1367–1382.e17 (2020).
54. P. S. Arunachalam *et al.*, *Nature* **594**, 253–258 (2021).
55. D. R. Martinez *et al.*, *Science* **373**, 991–998 (2021).
56. A. A. Cohen *et al.*, *Science* **371**, 735–741 (2021).

ACKNOWLEDGMENTS

Funding: Supported by National Institute of Allergy and Infectious Diseases grants DP1AI158186 and HHSN272201700059C (D.V.), a Pew Biomedical Scholars Award (D.V.), an Investigators in the Pathogenesis of Infectious Disease Awards from the Burroughs Wellcome Fund (D.V.), Fast Grants (D.V.), NIH grant S10OD032290 (D.V.), the University of Washington Arnold and Mabel Beckman Cryo-EM Center, and Wellcome Trust grant 209407/Z/17/Z. D.V. is an Investigator of the Howard Hughes Medical Institute. Beamline 4.2.2 of the Advanced Light Source, a US DOE Office of Science User Facility under contract DE-AC02-05CH11231, is supported in part by the ALS-ENABLE program funded by National Institute of General Medical Sciences grant P30 GM124169-01. For the purpose of open access, the author has applied a CC BY public copyright license to any Author Accepted Manuscript version arising from this submission. **Author contributions:** M.M., J.E.B., A.C.W., H.W.V., D.C., G.S., and D.V. conceived the project; M.M., L.E.R., S.K.Z., G.S., and D.V. designed experiments; M.M., N.C., S.K.Z., J.E.B., A.J., J.R.D., and A.E.P. expressed and purified proteins; L.E.R. and J.R.D. performed SPR analysis; S.K.Z. performed biolayer interferometry analysis; M.M. carried out cryo-EM sample preparation, data collection, and processing; M.M. and D.V. carried out cryo-EM model building and refinement; N.C. and J.R.D. carried out crystallization experiments; J.N. collected and processed x-ray diffraction data; M.M., T.I.C., G.S., and D.V. built and refined the crystal structure; and M.M. and D.V. wrote an initial draft of the manuscript with input from all authors. **Competing interests:** N.C., L.E.R., J.R.D., A.E.P., H.W.V., D.C., and G.S. are employees of Vir Biotechnology Inc. and may hold shares in Vir Biotechnology Inc. D.C. is currently listed as an inventor on multiple patent applications, which disclose the subject matter described in this manuscript. A.C.W., G.S., D.C., and D.V. are listed as inventors on patent 49230.03US1 describing the S309 epitope. H.W.V. is a founder and hold shares in PierianDx and Casma Therapeutics. Neither company provided resources. The Veesler laboratory has received a sponsored research agreement from Vir Biotechnology Inc. T.C.'s contribution was made under terms of a paid consultancy from Vir Biotechnology Inc. The remaining authors declare that the research was conducted in the absence of any commercial or financial relationships that could be construed as a potential conflict of interest. **Data and materials availability:** The cryo-EM map and coordinates have been deposited to the Electron Microscopy Databank and Protein Data Bank with the following accession numbers: 2 open/1 closed RBD EMD-25993; 2 closed/1 open RBD EMD-25992, EMD-25990, EMD-25991, PDB numbers 7TM0, 7TLY, 7TLZ. The crystal structure has been deposited to the Protein Data Bank with accession number 7TN0. Materials generated in this study will be made available on request, but we may require a completed materials transfer agreement signed with Vir Biotechnology or the University of Washington. This work is licensed under a Creative Commons Attribution 4.0 International (CC BY 4.0) license, which permits unrestricted use, distribution, and reproduction in any medium, provided the original work is properly cited. To view a copy of this license, visit https://creativecommons.org/licenses/by/4.0/. This license does not apply to figures/photos/artwork or other content included in the article that is credited to a third party; obtain authorization from the rights holder before using such material.

SUPPLEMENTARY MATERIALS

science.org/doi/10.1126/science.abn8652
Materials and Methods
Figs. S1 to S7
Tables S1 to S3
References (*57*–*77*)

View/request a protocol for this paper from *Bio-protocol*.

24 December 2021; accepted 20 January 2022
Published online 25 January 2022
10.1126/science.abn8652

Science

Structural basis of SARS-CoV-2 Omicron immune evasion and receptor engagement

Matthew McCallumNadine CzudnochowskiLaura E. RosenSamantha K. ZepedaJohn E. BowenAlexandra C. WallsKevin HauserAnshu JoshiCameron StewartJosh R. DillenAbigail E. PowellTristan I. CrollJay NixHerbert W. VirginDavide CortiGyorgy SnellDavid Veesler

Science, 375 (6583), • DOI: 10.1126/science.abn8652

Ongoing adaptation of SARS-CoV-2

Two years into the COVID-19 pandemic, several variants of severe acute respiratory syndrome coronavirus 2 (SARS-CoV-2) have arisen that show increased infectivity or evade immunity. The Omicron variant of concern has 37 mutations in the spike protein, which is responsible for host cell entry. Most of these mutations are in two domains targeted by neutralizing antibodies, the receptor-binding domain (RBD), and the N-terminal domain (NTD). McCallum *et al*. present structures of the viral spike bound to S309, a therapeutic antibody that maintains neutralizing activity against Omicron, and structures of the RBD bound to S309 and the human ACE2 receptor. The structures show how Omicron retains high-affinity binding to ACE2 while greatly reducing binding to other therapeutic antibodies. —VV